Title

Topographic hydro-conditioning to resolve surface depression storage and ponding in a fully distributed hydrologic model.

Authors

Hsu, Kuolin

Sanders, Brett

Jiang, Ai-Ling

et al.

Publication Date

2023-06-01

DOI

10.1016/j.advwatres.2023.104449

Peer reviewed

HHS Public Access

Author manuscript

Adv Water Resour. Author manuscript; available in PMC 2024 June 01.

Published in final edited form as:

Adv Water Resour. 2023 June ; 176: . doi:10.1016/j.advwatres.2023.104449.

Topographic hydro-conditioning to resolve surface depression storage and ponding in a fully distributed hydrologic model

Ai-Ling Jiang[a,*], **Kuolin Hsu**[a], **Brett F. Sanders**[b,c], **Soroosh Sorooshian**[a,d]

[a]Center for Hydrometeorology and Remote Sensing, Department of Civil and Environmental Engineering, University of California, Irvine, Irvine, CA, USA

[b]Department of Civil and Environmental Engineering, University of California, Irvine, Irvine, CA, USA

[c]Department of Urban Planning and Public Policy, University of California, Irvine, Irvine, CA, USA

[d]Department of Earth System Science, University of California, Irvine, Irvine, CA, USA

Abstract

Land surface depressions play a central role in the transformation of rainfall to ponding, infiltration and runoff, yet digital elevation models (DEMs) used by spatially distributed hydrologic models that resolve land surface processes rarely capture land surface depressions at spatial scales relevant to this transformation. Methods to generate DEMs through processing of remote sensing data, such as optical and light detection and ranging (LiDAR) have favored surfaces without depressions to avoid adverse slopes that are problematic for many hydrologic routing methods. Here we present a new topographic conditioning workflow, Depression-Preserved DEM Processing (D2P) algorithm, which is designed to preserve physically meaningful surface depressions for depression-integrated and efficient hydrologic modeling. D2P includes several features: (1) an adaptive screening interval for delineation of depressions, (2) the ability to filter out anthropogenic land surface features (e.g., bridges), (3) the ability to blend river smoothing (e.g., a general downslope profile) and depression resolving functionality. From a case study in the Goodwin Creek Experimental Watershed, D2P successfully resolved 86% of the ponds at a DEM resolution of 10 m. Topographic conditioning was achieved with minimum impact as D2P reduced the number of modified cells from the original DEM by 51% compared to a conventional algorithm. Furthermore, hydrologic simulation using a D2P processed DEM

[*]Corresponding author. jiangal@uci.edu (A.-L. Jiang).

Code availability

The codes developed for this work are available on GitHub along with the DEM used for the simulations: https://github.com/ailingjiang/D2P.

CRediT authorship contribution statement

Ai-Ling Jiang: Conceptualization, Methodology, Software, Validation, Formal analysis, Writing – original draft. **Kuolin Hsu:** Conceptualization, Writing – review & editing, Supervision, Funding acquisition. **Brett F. Sanders:** Conceptualization, Writing – review & editing. **Soroosh Sorooshian:** Conceptualization, Writing – review & editing, Funding acquisition.

Declaration of Competing Interest

The authors declare that they have no known competing financial interests or personal relationships that could have appeared to influence the work reported in this paper.

Supplementary materials

Supplementary material associated with this article can be found, in the online version, at doi:10.1016/j.advwatres.2023.104449.

resulted in a more robust characterization on surface water dynamics based on higher surface water storage as well as an attenuated and delayed peak streamflow.

Keywords

Surface depressions; Topographic processing; Hydrologic modeling; Digital elevation model

1. Introduction

Surface depressions have a direct impact on surface and subsurface flows through hydrologic, biochemical and biological exchanges (Cohen et al., 2016). Primarily, runoff can be modulated and delayed by surface depressions through fill-spill dynamics and storage effect (Ameli and Creed, 2017; Brooks et al., 2018). This has been shown to improve downstream water quality and support habitat functions because of longer residence times (Biggs et al., 2017; Cheng and Basu, 2017; Jones et al., 2018). In addition, large scale surface depressions in the form of wetlands and lakes can be critical for water supply as they replenish aquifers through seepage during dry conditions (Liu et al., 2016).

With a growing emphasis on the impact of surface depressions on hydrologic processes, semi-distributed hydrologic models have been widely used to provide new insights (Evenson et al., 2016; Wang et al., 2021). One approach is to aggregate surface depressions within each subbasin into a lumped depression that functions conceptually as a bucket. Water is stored in the bucket and spills as runoff when it exceeds a parameterized threshold volume (Hay et al., 2018; Liu and Schwartz, 2011; Rajib et al., 2020). This type of approach is simple to implement but fails to account for the spatial distribution of the depressions. In reality, some surface depressions may fill and contribute runoff water earlier than the others but in the lumped approach, water is only released to the streams when all the surface depressions (i.e., the aggregated depression) are fully filled. The other approach is to model surface depressions as individual units which better represents wetlands and their hydrologic connectivity. For example, Chu et al. (2013) developed a puddle-to-puddle (P2P) model where the study domains were divided into multiple puddle-based units (PBU). Each PBU contains the highest-level puddle and its contributing area. The PBU can drain to a downstream PBU based on an overflow threshold and the same applies for its embedded lower-level puddles based on a puddle delineation (PD) algorithm (Chu et al., 2010). Building on the PD algorithm and PBU concept, subsequent improvements were made to account for infiltration and unsaturated flow (Yang and Chu, 2015), improve the channel-puddle cascading mechanism (Nasab et al., 2017) and enhance computational efficiency (Wang and Chu, 2020).

Fully distributed hydrologic models have different needs for topographic data compared to semi-distributed models, given that the former is designed to resolve flow paths along and into the land surface (Golden et al., 2014), which in turn supports numerous geophysical applications such as material transport and reactive flows (Golden et al., 2017, 2014; Jones et al., 2019). In particular, fully distributed models require careful attention to spatial distribution of land surface heights as this drives the spatiotemporal variability of land

surface storage, infiltration, runoff and soil moisture (Amado et al., 2018; Liu et al., 2016). Hence, fully distributed hydrologic modeling at fine resolution calls for careful attention to the source of topographic data, which is generally supplied by a Digital Elevation Model (DEM) (Gardner et al., 2018; Jan et al., 2018; Tavares da Costa et al., 2019).

DEMs are developed in many different ways, but fine-resolution DEMs used in hydrologic modeling are typically derived from aerial LiDAR data or optical data with photogrammetric methods (Lidberg et al., 2017). Raw point cloud data is filtered to differentiate ground surface points from vegetation canopy, and then gridded to produce a preliminary DEM. Subsequently, DEMs are hydro-conditioned (i.e., filling or breaching topographic cells) to limit variability or noise in land surface slopes for smoother flow routing (i.e., lower chance of computational instability) (Chow and Ben-Zvi, 1973; Rieger, 1998; Zhang and Cundy, 1989), yet this process often removes physical land surface depressions that are highly relevant to hydrologic processes at the land surface. Previous studies have worked to identify land surface depressions for the purpose of characterizing the location and size of land surface features such as wetland and karsts (Bertassello et al., 2020; Li et al., 2011; Moreno-Gómez et al., 2019; Wu et al., 2016), but these work did not focus specifically on creating a DEM suited to resolving fine-scale land surface processes with spatially distributed hydrologic models. Hence, the objective of this study is to present a novel topographic processing workflow, referred to as Depression-Preserved DEM Processing (D2P) algorithm, with the aim of resolving surface depressions based on the scale of interest and smoothing small scale, non-physical variability in DEMs (e.g., Sanders, 2007) for depression-integrated and efficient modeling of land surface hydrology.

Our approach is designed for hydrologic models that calculate flow across 4 cell faces (i.e., D4) but can be modified easily to handle more flow directions (e.g., D8). Alongside a processed DEM, the algorithm also generates slopes across the cell faces. This adds to the limited number of DEM processing algorithms that can generate slope inputs for D4 routing models using finite difference methods (Condon and Maxwell, 2019). In this study, we detail the workflow of D2P and examine its utility in processing the DEM as an input for the integrated hydrologic model ParFlow (Ashby and Falgout, 1996; Jones and Woodward, 2001; Kollet and Maxwell, 2006; Maxwell, 2013). We compare the processed DEM and evaluate the hydrologic simulation against the traditional filling method by Condon and Maxwell (2019) using a case study on the Goodwin Creek Experimental Watershed (GCEW).

2. Materials and methods

2.1. Study area

GCEW is located in northern Mississippi, United Statesand the area of the watershed is 21.7 km^2, with an elevation ranging from 64.8 m to 129.1 m above mean sea level (Fig. 1). The land use is mainly idle pasture, followed by forest and cultivated land and there is a high density of small water bodies such as farm ponds (Yasarer et al., 2018). Based on the satellite imagery from the National Wetlands Inventory (NWI) provided by United States Fish and Wildlife Service (USFWS) (https://www.fws.gov/wetlands/), there are a total of 93 fresh water ponds ranging in size from 500 m^2 to 11,000 m^2.

The DEM used in this study was downloaded from a derived-LiDAR product by the Mississippi Automated Resource Information System. The DEM represents bare earth surface that was created from LiDAR points collected from 2009 to 2010 by the U.S. Army Corps of Engineers (USACE) for the Mississippi Delta Phase 1 project (https://www.maris.state.ms.us/HTML/DATA/Elevation.html#gsc.tab=0) and was hydroflattened. The spatial resolution is 1 m and the vertical accuracy is 0.09 m (Root Mean Square Error). The DEM was first smoothed by a median filter to remove roughness and aggregated to 10 m resolution to keep the hydrologic simulation computationally manageable.

2.2. Overview of Depression-Preserved DEM Processing (D2P) algorithm

The D2P algorithm comprises six steps as shown in the flowchart in Fig. 2. Using DEM and NWI wetland as input data, it identifies surface depressions that are likely to be physically meaningful and generates a processed DEM that is smoothened to reduce fine scale variability while preserving those depressions. Slope data is then derived from the processed DEM. Details of steps 1 to 6 of the flowchart are explained from Sections 2.2.1 to 2.2.6.

2.2.1. Topographic sink extraction—A depression-less DEM was first obtained by filling the sinks using Priority-Flood, a depression-filling tool (Barnes et al., 2014). All the topographic depressions comprising real depressions and artifacts were then extracted by subtracting the input DEM from the depression-less DEM. The artifacts are caused by systematic and random errors from the precision of data acquisition instrument and processing techniques (Zhu et al., 2013).

2.2.2. Removal of small-scale depressions in DEM—From the extracted topographic depressions (Section 2.2.1), an improved adaptation of the level set method (Wu et al., 2019) was applied to characterize the depressions in terms of their geometric properties and hierarchy. A depression hierarchy describes the relationship between each depression whereby depressions can themselves contain smaller ones. The most-nested depression is referred to as a Level 1 depression and the level increases as the depressions combine to form bigger depressions (Supporting Information Text S1).

The level-set method by Wu et al. (2019) establishes the hierarchy by screening each depression from the highest elevation and moving downwards to determine the spill point at which depressions combine (Supporting Information Text S2). One disadvantage of this method is that the screening was performed at fixed intervals and could overlook certain depressions (Barnes et al., 2019). To avoid this, the screening interval must be reduced but the computation can become inefficient (Supporting Information Text S3). Therefore, we modified the method to screen at each unique DEM cell elevation within the depression instead of at fixed intervals. This ensures that each depression is assigned the correct level in the hierarchy. The level of each depression will be used in Section 2.2.4.

After establishing the hierarchy, the area of each depression was determined and the average depth of each depression, D, was calculated using Eq. (1).

$$D = \sum_{i=1}^{n} (z_s - z_i)/n$$

where n is the number of DEM cells within the depression, z_s is the spill elevation and z_i is the elevation of the i^{th} cell in the depression. Finally, average depth and area thresholds of 0.0036 m and 900 m^2 were applied. The motivation of the thresholds was to identify and remove small-scale depressions that are deemed to be inconsequential to the overall hydrologic process since they tend to fill easily and lose their function as closed basins in most rainfall events (Li et al., 2011). The thresholds also help to filter out small-scale non-physical variabilities from the DEM to improve computational efficiency. These small-scale depressions were removed by filling to generate a modified DEM. The thresholds were derived from a sensitivity assessment of the final delineated depressions using different threshold values to achieve a balance between matching the wetland data from NWI and excessive false matches (Supporting Information Text S4). The considerations for the setting of the thresholds are also discussed in Section 4.1

2.2.3. Watershed analysis—The watershed analysis was implemented using the GRASS module, r.watershed (GRASS Development Team, 2020). An A* least-cost search algorithm (Hart et al., 1968; Metz et al., 2011) was applied on the modified DEM from 2.2.2 to generate flow direction and river network. This algorithm does not require the DEM to be further altered to determine flow direction and extracts the path of rivers through depressions more accurately compared to traditional methods (Planchon and Darboux, 2001; Wang and Liu, 2006) with sink filling (Metz et al., 2011).

2.2.4. Classify riverine depressions for targeted preservation—In this section, we focus on riverine depressions after having removed small-scale depressions from the DEM (Section 2.2.2). DEMs are especially prone to errors along rivers due to the difficulty of sensors in penetrating thick riparian vegetation and water bodies as well as the resolution limits in resolving the channel bottom elevation (Lindsay, 2016a; Schwanghart and Scherler, 2017). This creates spurious topographic variability along rivers leading to depressions inside the channel width with discontinuous bottom slopes that can cause model instability (Hengl, 2006; Iserles, 2009; Yu et al., 2020). In addition, high resolution LiDAR-derived DEMs can contain false hydrologic barriers such as bridges or roads (Carlson and Danner, 2010) that will form false depressions during the depression extraction process in Section 2.2.1. Such false depressions are rarely addressed in previous depression-integrated studies.

Hence, our goal is to filter out the aforementioned spurious depressions within the channel width (Fig. 3a) and depressions arising from false hydrologic barriers (Fig. 3b) to finally keep the remaining water bodies that partially coincide with rivers (Fig. 3c). To achieve this, we developed a new metric that takes advantage of the hierarchy of depression levels. The metric, referred herein as the river to depression ratio (*RtD*), provides a measure of the contribution of the river to the makeup of the depression. The *RtD* was calculated for each highest-level depression using the formula in Eq. (2).

$$RtD = \left(\frac{n_r}{n}\right)\left(\frac{n_{L_1,r}}{n_{L_1}}\right) \quad (2)$$

In Eq. (2), n is the number of DEM cells within the highest-level depression and n_r is a subset number of cells from n that are within the river channel width; while n_{L_1} is the number of DEM cells in all Level 1 depressions (i.e., the most nested depressions) within the highest-level depression and $n_{L_1,r}$ is a subset number of cells from n_{L_1} that are within the river channel width. The equation is a product of two ratios. The first ratio is a measure of the extent of the depression that coincides with the river. The higher the first ratio, the larger the portion of the depression falling within the river channel width (Fig. 3a). The second ratio was introduced to specifically distinguish between false depressions arising from roads or bridges and actual water bodies that partially coincide with the river. It does so by drawing on the depression hierarchy from Section 2.2.2 to gage the geometry of the depression. Ponds and wetlands generally have a bowl-like structure with a flat bottom which manifests itself by the Level 1 cells spreading beyond the river, resulting in a lower $n_{L_1,r}/n_{L_1}$ (Fig. 3c). On the other hand, in false depressions arising from road or bridge crossings, Level 1 cells are mostly concentrated within the river channel width, resulting in a higher $n_{L_1,r}/n_{L_1}$ (Fig. 3b).

Using Eq. (2), depressions with RtD lower than a certain threshold would be selected for preservation in the next section as their geometry suggests that they are more likely to be physically meaningful depressions that intersect with a river (e.g. Fig. 3c). In other words, the threshold is the maximum RtD for a physically meaningful depression in the study area. To determine the threshold, the RtD was calculated for each depression from NWI data and the maximum calculated RtD was set as the threshold.

By this point, we had identified physically meaningful depressions that we wanted to preserve in the DEM. The preserved depressions compared well against the wetlands in the NWI data (Fig. 4). The excluded depressions, namely small-scale depressions, depressions within the channel width and depressions associated with false hydrologic barriers were all assumed to be artifacts.

2.2.5. River network smoothening—We applied a quantile regression algorithm to smoothen the river while preserving the depressions partially coinciding with the river identified in Section 2.2.4. The smoothening aims to maintain the general profile while reducing fine scale variability and adverse slopes. Previous studies smoothen the river profile by modifying the elevation universally based on the average slope of the reach (Barnes et al., 2016; Condon and Maxwell, 2019). The approach we adopt here offers the flexibility to process the river segment intersecting with depression differently from other segments.

Generally, the algorithm works by minimizing the sum of absolute values of the residuals given by the difference between the smoothened elevation and the raw elevation as well as the roughness. The underlying optimization function of the algorithm, known as the

constrained regularized smoothing (CRS) algorithm, is shown in Eq. (3) (Schwanghart and Scherler, 2017).

$$\arg\min \sum_{i=1}^{n} (\rho_\tau(z(x_i) - \mathbf{I}z_\tau(x_i))) + s \int \left[z_\tau^{''}(x)\right]^2 \mathrm{dx} \tag{3}$$

where $z(x_i)$ is the unsmoothed elevation along river profiles x distance upstream of the watershed outlet, n is the number of elevations, $\mathbf{I}$ is the identity matrix, $\tau \in [0, 1]$ is the constant chosen according to which quantile needs to be estimated. In this case, τ was set at 0.5. z_τ is the estimated elevation. $\rho_\tau(\cdot)$ is a loss function dependent on the residuals r_i given by

$$\rho_\tau(r_i) = (\tau - \|_{r_i < 0}) r_i \tag{4}$$

where r_i is defined as $z(x_i) - \mathbf{I}z_\tau(x_i)$ and $\|$ is an indicator function that has a value of 1 if the residual r_i is less than 0 and a value of 0 otherwise. s dictates the degree of smoothening and is defined by

$$s = (\Delta x)^2 K \sqrt{\frac{n}{p}} \tag{5}$$

where Δx is the resolution of the DEM, p is the number of second derivative terms in Eq. (3), K is the parameter that scales the degree of smoothing.

In Schwanghart & Scherler (2017), the river profile was forced to decrease in the downstream direction and the degree of smoothening s was set to be uniform throughout the entire river network. To avoid distorting the actual depressions that intersect the river path (e.g. Fig. 3c), we introduced separate conditions to process river segments within depressions and river segments outside of depressions. For river segments outside depressions, the downstream elevation was forced to be lower than the upstream by a minimum difference ε as shown in Eq. (6)

$$z_\tau(x) \geq z_\tau(x - \delta x) + \varepsilon \tag{6}$$

This was not applied for river segments inside depressions to avoid removing the depressions. In addition, s was set to be higher for river segments outside of depressions but lower in river segments within depressions to preserve any high curvature structures (e.g., dams) downstream of the depressions.

Lastly, to prevent the river cell being raised inadvertently creating depressions outside the river, we introduced a new condition whereby the elevation of the river segment was globally set not to exceed that of the riverbanks by ε.

$$z_\tau(x) \leq \min(z_{\tau, y+\delta y}(x), z_{\tau, y-\delta y}(x)) - \varepsilon \tag{7}$$

Fig. 5 illustrates the different constraints that were imposed on the river segments within the depressions and outside the depressions. The modified algorithm will be referred to as the adapted CRS algorithm. Following the implementation of the adapted CRS algorithm, we temporarily masked out the stream segments and preserved depressions and applied filling on any sinks created as a by-product in the DEM (Barnes et al., 2014). A final processed DEM was obtained.

2.2.6. Slope calculation—The outcome of the above steps was a processed DEM with smoothened rivers and retained depressions. In this step, slopes in the north-south and east-west directions were calculated for each cell. The north-south slope is defined at the upper cell face between a cell and the adjacent cell to the north while the east-west slope is defined at the right cell face between a call and the adjacent cell to the east. The calculated slope direction for cells outside of depressions was adjusted to match the flow direction by reversing the sign whenever there was a discrepancy. The slope magnitude remained unchanged but subject to a maximum slope threshold and a minimum slope threshold.

2.3. Comparative analysis

To assess the performance of D2P, we evaluated the extent and magnitude of its modification on the raw DEM and the subsequent impact on overland flow. Since ParFlow is used in this study, we chose PriorityFlow (Condon and Maxwell, 2019), a recent DEM conditioning algorithm developed for ParFlow, to be compared against D2P. The algorithm followed the traditional way of removing all the sinks and the approach is justified when a kinematic wave approximation is used for the overland flow simulation.

DEM processing algorithms are known to introduce errors since it is difficult to ascertain the origin of each depression so the algorithm should ideally achieve a reasonable flow path with minimal modification to the DEM (Lindsay and Creed, 2005). Hence, we quantified the change in elevation of the processed DEM relative to the source DEM as a measure of the change to the landscape. In addition, we performed a rainfall recession simulation in ParFlow using the processed DEMs and the raw DEM by applying a rainfall rate of 5 mm/hr for 10 hrs followed by 20 hrs of recession, similar to the test used by Barnes et al. (2016) and Condon and Maxwell (2019) The simulation was performed on an impervious surface to focus on surface water processes. Diffusive wave approximation was used for overland flow.

Table 1 summarizes the five DEMs that were used in the comparative study. The raw DEM, the processed DEM from the conventional algorithm and the processed DEM from D2P are represented by Case 0, Case 1 and Case 4, respectively. Case 1 fills the depressions first and smoothens the river by enforcing a constant average slope between two ends of each reach. Due to the fundamental differences between the conventional algorithm and D2P in terms of the treatment of the depression and river smoothening, two cases were added to isolate the effect of each change on the DEM from Case 1 to Case 4. Case 2 changes the river smoothening in Case 1 to the use of the adapted CRS with the uniform constraint of elevation decreasing downstream (Eq. (6)). Case 3 uses the adapted CRS with uniform constraint of elevation decreasing downstream before filling. Case 3 is the closest to Case

4 in terms of the processed DEM except that select depressions are preserved during the adapted CRS step and the filling step in Case 4.

In summary, Cases 1 to 3 condition DEMs using different combination of depression treatment and stream smoothening methods without preserving any depression, while Case 4 incorporates select depressions. An example of a processed river segment from Case 0 to Case 4 is illustrated in Supporting Information Fig. S9.

3. Results

3.1. Evaluation of identified depressions

To evaluate the accuracy of the delineated depressions by D2P algorithm, 1-m resolution aerial imagery from the National Agriculture Imagery Program (NAIP) (https://www.fsa.usda.gov/programs-and-services/aerial-photography/imagery-programs/naip-imagery/) was used to manually delineate the ponds as a benchmark for comparison. The imagery was chosen from July 2009 to match the date of the LiDAR DEM used in this study. Alongside the DEM resampled to 10-m resolution, the comparison was also done at the original LiDAR DEM resolution of 1 m and two other resampled resolutions of 5 m and 20 m. The area and depth thresholds are set the same for all the resolutions to solely investigate the impact of DEM resolution on depression identification.

From Fig. 6a–d, the D2P algorithm was able to identify at least 85% of the delineated ponds from the NAIP imagery (56 out of 66) at the DEM resolutions of 1 m, 5 m and 10 m but the performance dropped to 35% (23 out of 66) at the coarsest resolution of 20 m. This indicates the inability of the 20-m resolution DEM to resolve the scale and geometry of the depressions in the study area. Most of the NAIP ponds had an area of the same order of magnitude (~400 m^2 to 4000 m^2) as the 20 m by 20 m grid cell so the depressions in the DEM could easily be lost during the resampling of the DEM. We compared the area of the depressions identified by D2P against the NAIP ponds and found a close agreement, with a coefficient of determination (R^2) of at least 0.75 across all the resolutions. In general, there is an overestimation in the area of the depressions delineated by D2P as shown in Fig. 6e. This is because the D2P depression area is determined by filling the depressions in the raw DEM up to the spill point elevation, which makes it the maximum possible area. The manually delineated areas from NAIP reflect the state of the pond at a specific time but may not be the maximum given the tendency to fluctuate depending on the climate. Moreover, vegetation and shadows in the NAIP imagery may mask the true boundary of the ponds during manual delineation and result in underestimation of the pond extent (Yasarer et al., 2018). Notably, the positive bias tends to increase with the DEM resolution because the DEM at higher resolution is better able to represent the boundary of the maximum depression area more closely. On the other hand, a coarser resolution DEM may fail to capture the irregular boundary of the depression and underestimate the area, as is the case for the 20 m DEM especially for the smaller ponds.

Another statistical analysis in the form of the binary pattern metrics shown in Table 2 was conducted to further examine the degree to which the D2P depressions agree with the NAIP ponds in terms of location and extent. The results affirmed the performance of D2P as the

probability of detection (POD) indicated that more than 85% of the depressions matched the ponds for DEM resolutions 10 m and lower. D2P produced false alarms across all four DEM resolutions, with the false alarm rate (FAR) ranging from 44% to 53%. This is to be expected due to the tendency to overestimate the depression area as explained previously and the fact that not all depressions may result in the formation of a pond. In general, as the DEM resolution increases, the POD increases but this is offset by an increase in the FAR, so the resulting critical success index (CSI) is similar for the DEM resolutions of 1 m, 5 m and 10 m at about 50%. However, at the DEM resolution of 20 m, we observe that the POD drops drastically but the FAR does not decrease in tandem and this causes the CSI to decrease significantly to 32%.

From the above comparisons, we have shown that D2P is able to reasonably identify depressions provided that the DEM resolution is able to resolve the scale of the depressions of interest. While D2P will perform better in capturing both the location and geometry of the known depressions from existing datasets (e.g., NWI, NAIP) with a higher resolution DEM, it also generates a higher number of unknown depressions, which can be hard to validate without ground truth data.

3.2. Effect of processing methods on DEM

The extent and magnitude of the impact to the raw DEM by the different methods decreased gradually from Case 1 to Case 4, as shown by the percentage of modified cells and mean absolute elevation offset in Table 3. This agrees with previous research (Lindsay, 2016b) which showed filling (Case 1 and Case 2) to have a bigger impact on the DEM than a hybrid of breaching and filling (Case 3 and Case 4). Between Case 4 and Case 1, D2P reduced the percentage of modified cells for the entire watershed from 11.3% to 5.58% and the mean absolute elevation offset by 5-fold from 0.0745 m to 0.0145 m compared to the conventional algorithm.

Focusing on the river network which was more likely to have changed due to the additional smoothing step, the elevation of practically all the cells in Case 1 were modified compared to only 30.6% of the cells in Case 4. In addition, the magnitude of modification was also smaller in Case 4, with a mean absolute elevation offset of 0.223 m compared to 0.648 m in Case 1. From the boxplot in Fig. 7, there was a predominant increase in elevation in Case 1 and Case 2 but not Case 3 and 4 due to the nature of the filling algorithm. At the same time, the elevation offsets were highly variable in Case 1 (−1.5 m to +2 m) and Case 2 (−0.6 m to +1 m) compared to Case 3 (−0.4 m to +0.4 m) and Case 4 (−0.4 m to +0.4 m). Overall, the differences between the river profile from the processed DEM and the raw DEM were the highest in Case 1 followed by Case 2 and finally Cases and 3 and 4 which were similar.

3.3. Effect of processing methods on hydrologic simulation

To understand the impact of the processing methods on hydrologic simulation, we compared the distribution of the simulated surface water depth and the time series of the surface water storage and streamflow. Fig. 8 shows the instantaneous surface water depth distribution for a selected location in the watershed with a high density of ponds. 10 hrs into the simulation at the end of the heavy rainfall (Fig. 8c), the location and extent of the ponds in both Case

0 and Case 4 generally matched that of the ponds extracted from NAIP. However, artifactual depressions could be observed in Case 0 such as the one in the black circle as a result of using the raw DEM. This is a classic example of a false depression arising when a road crosses over the river. In Cases 1, 2 and 3, the depression removal process created flat terrain in the NAIP pond areas, resulting in minimal accumulation of water less than 0.1 m in depth. Notably, Case 1 resulted in a larger flooded area compared to Cases 2 and 3 as the elevation of the river profile was raised gradually upstream to maintain a constant slope, thereby reducing the capacity of the channels.

30 hrs into the simulation at the end of the recession (Fig. 8d), the residual water in flat areas in Cases 1 to 3 had already dried out. On the other hand, the depressions in Case 4 functioned as storage by trapping the water and formed isolated ponds. The result was not available for Case 0 as the model stopped running at the 11^{th} hour due to the numerical instability from using the raw DEM. Overall, the DEM in Case 4 allowed ponding to be modeled realistically and the choice of DEM processing resulted in significant difference in the spatial distribution of ponding. Refer to Supporting Information Fig. S10 for a similar comparison at another location within the watershed.

Next, we analyzed the surface water storage time series for all cases. The total surface water storage (Fig. 9a) was broken down into a river storage component (Fig. 9b) and a non-river storage component (Fig. 9c).

In Fig. 9a, the total surface water storage was highest in Case 0 up to the point when the model terminated prematurely. This is because the drainage was poorest in Case 0 due to the lack of a smoothened river network that could direct water to flow between cell faces. The water from the rainfall became trapped in sinks and could barely reach the outlet of the watershed. Of the other cases, the total surface water storage was highest in Case 4 due to retention of water by the preserved depressions. Although the total surface water storage was similar across all depression-less simulations (i.e., Cases 1, 2 and 3), the choice of river smoothening mechanism and depression treatment resulted in a large difference in the distribution of storage between the river and non-river components. In Fig. 9b, the river storage was lower in Cases 1 and 2 than Case 3. This can be attributed to the shallower channel depth (See Table 4) from the use of filling to remove depressions in Cases 1 and 2. Conversely, the shallower channel depth makes the river more prone to overflowing and results in a higher non-river surface water storage in Case 1 and 2 compared to Case 3 (Fig. 9c).

By preserving and integrating depressions in the hydrologic simulation, the river storage in Case 4 was reduced compared to Case 3 (Fig. 9b) because surface runoff was intercepted as non-river storage. After the rain had stopped, the non-river storage in Case 4 decreased much slower than other cases due to the retention effect of the depressions.

Fig. 10 shows the hydrographs at the outlet of the watershed. Without any DEM processing, the peak flow was substantially lower in Case 0 as it was difficult for the water to flow past the rugged terrain to the outlet of the watershed. This corresponds with the behavior of storage in Fig. 9 whereby most of the water arriving as rainfall remained as surface water

storage after getting trapped by the sinks until the 10th hr. The streamflow took about the same time to peak for Cases 1, 2 and 3. However, the peak streamflow in Case 3 was visibly higher than Case 1 and Case 2 because of the higher flow depth at the outlet. Comparing Case 4 and Case 3, an attenuation of the peak streamflow was observed in the former due to the preserved depressions. The peak stream flow in Case 4 was reduced by 10% compared to Case 3 and the hydrograph for Case 4 lagged that of Case 3 by 0.4 hr.

4. Discussion

4.1. Threshold for removal of artifacts

For this study, to distinguish farm ponds from depressions too small to be significant to the hydrologic simulation, we set a minimum threshold depression depth of 0.0036 m and area of 900 m^2 based on NWI data. There is not a universal value that can be applied to all cases and the threshold should ideally be determined based on the scale of interest, knowledge of the existing site, DEM resolution and computational efficiency of the hydrologic simulation.

For example, to investigate malaria vector habitat dynamics in Africa, the hydrologic model needs to consider smaller (~100 m^2) and shallower depressions (<0.5 m) as the dominant malaria vectors prefer transient pools for breeding (Minakawa et al., 1999). On the other hand, the threshold will be very different for a reservoir simulation considering that the scale of the water body of interest is much bigger. Any existing site information will also be helpful in refining the thresholds. Guided by the Minnesota Karst Feature Database (KFDB), Wu et al. (2016) used a minimum depression area of 100 m^2 and minimum depression depth of 0.5 m to identify natural sinkholes. In a separate experiment conducted on the Prairie Pothole Region of North Dakota, a different threshold of a minimum depression size of 2000 m^2 and minimum depression depth of 0.3 m was chosen based on spatial data from US Geological Survey (Wu et al., 2019).

Area and depth thresholds can also vary with DEM resolution. From the sensitivity analysis in Supporting Information Text S4, the performance of the tested thresholds in the successful identification of wetlands from NWI data by D2P generally increased with DEM resolution. Higher resolution DEMs typically require larger area threshold as there is a higher probability of small artifactual depressions that need to be removed (Li et al., 2011). However, the same trend was not observed in our study. Instead, the optimal area threshold across the resolutions of 1 m, 5 m, 10 m were all around 800 m^2 to 900 m^2. This could be due to the quality and nature of the NWI data which is a record of wetlands and not all depressions in the study area. On the other hand, a lower depth threshold may be needed for lower resolution DEMs obtained by aggregating a higher resolution DEM. Aggregating a higher resolution DEM has the effect of averaging out the topographic variability, resulting in shallower depressions.

Another factor to consider is the trade-off between the realism of the topographic representation and computational efficiency. While setting a low threshold would allow the DEM to capture most of the depressions, it will also increase the variability in the topography which could inadvertently introduce slope discontinuities and develop oscillation and instability issues for some models. For instance, setting the threshold area too low

increases the chances of including deep yet small depressions that are anomalous and can greatly hurt the numerical performance.

Surface depressions within the channel width and depressions associated with false hydrologic barriers were removed based on a calculated *RtD* threshold. A threshold that is set too low causes more depressions intersecting with the river to be removed, including ponds and wetlands along rivers (Fig. 3c) that could serve important hydrologic functions. On the other hand, a higher threshold would cause more depressions intersecting with the river to be preserved, including false depressions arising from roads or bridges, and also result in a more rugged river profile. In this study, the threshold was inferred based on known depression locations from NWI data.

In general, the *RtD* threshold decreases as the resolution increases. The calculated *RtD* thresholds were 0.8, 0.54, 0.33 and 0.076 for DEM resolutions of 20 m, 10 m, 5 m and 1 m, respectively. This is due to the overestimation of the areal representation of the river at lower resolutions. The performance of the *RtD* threshold in distinguishing false depressions associated with roads or bridges from water bodies that coincide with the river drops as the resolution decreases. This is due to the inability of the DEM to fully resolve the depression hierarchy at lower resolutions. At 20-m DEM resolution, the FAR (Table 2) was particularly high which can be attributed to the inclusion of false depressions.

4.2. Implication of DEM processing algorithm on hydrologic simulation: filling vs hybrid

Many studies have compared the influence of different DEM processing algorithms on the DEM in terms of elevation, slope and hydrological attributes (Callow et al., 2007; Lindsay, 2016b; Lindsay and Creed, 2005; Woodrow et al., 2016). In line with those studies, our comparison across the four cases shows that the filling based algorithms in Case 1 and Case 2 produced a greater impact on the DEM quantified by the number of modified cells and elevation offset in Table 3 and Fig. 7. However, the impact of the DEM processing algorithms on the hydrological simulation is rarely discussed. From the rainfall recession simulation, we observe local differences in the pattern of the ponding between filling and hybrid algorithms, especially around false depressions arising from the crossing of a road over a river. In Case 1 and Case 2, filling raised the elevation of the upstream river valley to at least match the level of the road crossing, and this resulted in inundation over a large area upstream of the road crossing with relatively similar elevation. In extreme cases, the flat inundated area could create an obstruction to the incoming river and cause the flow to back up, increasing the computational demands. On the other hand, the hybrid algorithm in Case 3 breached the road crossing and allowed water to flow through the river channel relatively easily. In addition, we observe that both the filling and hybrid algorithms resulted in roughly similar mean channel slopes, but the former reduced the channel depth by 22% to 25% compared to the latter. This could cause overestimation of fluvial flooding as alluded to by the higher non-river storage in Fig 9c and potentially result in overly conservative flood management policies.

4.3. Implication of depression-integrated hydrologic simulation: depression vs depression-less

We show in our rainfall recession simulation that the inclusion of depression modified the hydrologic response of the watershed. We observe an attenuation in streamflow at the watershed outlet and increase in lag time of the hydrograph as the depressions stored some of the rainfall and delayed the arrival of runoff to the rivers. This mechanism is widely acknowledged by other similar studies (Nasab and Chu, 2020; Yasarer et al., 2018; Zeng et al., 2020). At the same time, by explicitly representing the depressions in the DEM, we present a viable means to capture the hydrologic connectivity between the depressions which is rarely achieved in the existing depression-integrated hydrologic models. The connectivity between ponds, headwater streams and downstream waters was evident in Case 4 at the end of the rainfall event in Fig. 8c. Long after the rainfall event when the supply of water had stopped, the connecting streams that were ephemeral in nature gradually dried up, resulting in geographically isolated ponds in Fig. 8d. This process was absent in Case 3 as there was no storage function with a depression-less DEM.

The impact of the depressions on the hydrologic response can vary with the magnitude of rainfall. To illustrate this, we increased the rainfall rate applied in the first 10 h of the simulation from 5 mm/hr to 10 mm/hr. As shown in Fig. 11, at 5 mm/hr rainfall rate, the total runoff volume (i.e. area under the hydrograph) in Case 4 is 14% lower than that of Case 3. At the higher rainfall rate of 10 mm/hr, the relative difference in total runoff volume reduces to 9%. This implies that the higher the rainfall intensity, the lower the impact of the depressions on the hydrologic response. The finding is consistent with the study by Costabile et al. (2022). One reason is because at the higher rainfall intensity, the depressions tend to fill up more easily and the storage volume becomes less significant compared to the runoff volume.

By accounting for depression storage in model simulations, it is possible to improve the accuracy of flood hazard studies and allow surface depressions to be leveraged as part of a holistic approach in mitigating flood risk and preventing overpredictions. Beyond flood hazard studies, depression integrated hydrologic modeling has the potential to augment water resources management by enhancing the spatial delineation of water across the watershed and providing a more effective guide for local irrigation and crop rotation strategies (Rajib et al., 2020). Lastly, it is feasible to explicitly represent the connectivity between depressions and streams in studies to understand the effects of the transport of materials and biological fluxes within aquatic ecosystems (Leibowitz et al., 2019).

4.4. Limitation of the algorithm

There are three main limitations to D2P. Firstly, the artifactual riverine depressions were removed if the *RtD* was below the threshold, which requires knowledge of locations of wetlands in the study area especially those that intersect with the river. In our case, we derived the *RtD* threshold from NWI data, which is only available within the United States. For future applications outside of the United States, there is a need to check the local database for similar information or resort to other means to determine the *RtD* threshold

such as through field survey. If the above is still not feasible, the threshold can be estimated iteratively by a sensitivity analysis.

Secondly, a D2P-processed DEM can result in higher computational demands in distributed hydrological modeling than depression-free DEMs. By comparing the number of solver iterations among the five cases in Fig. 12, Case 4 generally had a higher computational demand than Cases 1 to 3. The number of iterations increased sharply near the 5^{th} time step where the water was just starting to fill the depression. This process was harder to solve in ParFlow at the point when the overland flow component was activated. From the 7^{th} to 10^{th} timestep, Case 1 required the highest number of iterations than Cases 2 to 4. One possible reason was that the flat areas created by the filling process in Case 1 obstructed the incoming flow from the river and caused it to back up, increasing the computational demands. After the rain stopped, the surface water flow in Cases 1 to 3 decreased and became gradually easier to solve compared to Case 4 where water was retained by the depressions. Notably, the number of iterations required in Case 0 was substantially higher than the other cases, indicating that some degree of DEM processing was necessary for modeling purposes.

Finally, we note that hydro-conditioned DEMs produced by the D2P workflow are optimized for hydrologic routing methodologies that rely on topographic slopes, such as ParFlow. Consequently, D2P DEMs may not necessarily be optimal for hydrologic models that rely directly on topographic heights or in flood hazard simulation where the extent and depth of ponded areas are sensitive to certain topographic features along the river (Hodges, 2015; Sanders and Schubert, 2019). In Sections 2.2.4 and 2.2.5, we removed all depressions within the river channel width as shown in Fig. 3a as we could not distinguish artificial depressions from real features such as riffles and pools. However, the D2P workflow could be adapted to meet slightly different needs with respect to removing some features in the DEM and retaining others. For example, the *RtD* threshold can be adjusted higher to retain more stream depressions and exempt them from the enforcement of the downslope condition in the adapted CRS algorithm.

5. Summary and conclusions

Despite the growing emphasis on the impact of surface depressions on hydrologic processes, there is a lack of a formalized DEM processing tool that can resolve surface depressions of interest for fully distributed hydrologic modeling. To address this gap, we present the Depression-Preserved DEM Processing (D2P) algorithm, a novel automated workflow that provides a representation of the land surface consistent with hydrologic processes being resolved while removing small-scale, non-physical variability in the DEM for computational efficiency. To achieve the above, the D2P algorithm includes several features, namely (1) improved delineation of surface depressions by screening depressions at variable instead of fixed intervals, (2) adoption of a new metric, *RtD*, leveraging depression hierarchy to filter out artifactual riverine depressions and (3) adaptation of a hybrid approach to smoothen the river in a way that enforces the general downslope profile while preserving surface depressions that intersect the river path.

The application of the proposed algorithm in a case study in GCEW minimizes the modification to the original DEM and the identified depressions match well with the delineated ponds from NAIP imagery. The performance of D2P in identifying depressions was evaluated over four different resolutions of 1 m, 5 m, 10 m and 20 m. In addition, the use of the D2P-processed DEM in a distributed hydrologic model also highlights the difference that the incorporation of depressions makes to the simulated ponding, water storage and streamflow. Following are the conclusions drawn from the study:

1. The D2P algorithm was able to identify at least 85% of the delineated ponds from NAIP satellite imagery at the DEM resolution of 1 m, 5 m and 10 m but not at 20 m. The performance of D2P did not vary much as the DEM resolution decreased from 1 m to 10 m.
2. Compared to a conventional DEM processing algorithm which removes all the depressions, the D2P algorithm has a significantly lower impact on the raw DEM by reducing the percentage of modified cells for the entire watershed by 51% and the mean absolute elevation offset by 81%.
3. The hydrologic simulation for the rainfall recession test showcases the ability of D2P to capture the spatial distribution of physically meaningful depressions and their storage function. The depression-integrated simulation results in higher total surface water storage as well as an attenuated and delayed peak streamflow due to retention of water by the preserved depressions.

Although LiDAR DEMs are generally of high accuracy and can provide a good representation of the landscape, the direct use of the raw DEM in hydrologic models using topographic slopes to route flow results in significant computational demands. The proposed D2P algorithm provides a systematic means to balance the need to process DEM for ease of computation and the preservation of surface depressions of interest. While we have only demonstrated the application of D2P for small water bodies in GCEW, the algorithm can also be used to process DEMs in the context of larger water bodies such as Prairie Potholes. The choice of hydrologic model would have to be tailored to the nature and geometry of the water bodies of interest.

Our case study of a test rainfall event clearly suggests that the treatment of surface depressions and the choice of method for smoothening topographic variability (e.g., filling and breaching) have a significant influence on the hydrologic simulation results. D2P adopts a minimum impact approach to avoid distorting terrain attributes unnecessarily while offering the user flexibility in altering depressions under different settings. Future work involves testing and evaluating the D2P algorithms across different landscapes. D2P facilitates depression-integrated studies using more fully distributed hydrologic models like ParFlow. This can provide new insights into complex hydrologic systems and help improve water resources management and environmental sustainability decisions.

Supplementary Material

Refer to Web version on PubMed Central for supplementary material.

Acknowledgments

This work was supported by grants from National Institutes of Health (U19 AI129326), U.S. Department of Energy (HydroWIRES Initiative DE-EE0008943) and California Department of Water Resources (AR Program 4600013361).

References

Amado AA, Politano M, Schilling K, Weber L, 2018. Investigating hydrologic connectivity of a drained prairie pothole region wetland complex using a fully integrated, physically-based model. Wetlands 38, 233–245. 10.1007/S13157-016-0800-5.

Ameli AA, Creed IF, 2017. Quantifying hydrologic connectivity of wetlands to surface water systems. Hydrol. Earth Syst. Sci 21, 1791–1808. 10.5194/hess-21-1791-2017.

Ashby SF, Falgout RD, 1996. A parallel multigrid preconditioned conjugate gradient algorithm for groundwater flow simulations. Nucl. Sci. Eng 124, 145–159. 10.13182/NSE96-A24230.

Barnes ML, Welty C, Miller AJ, 2016. Global topographic slope enforcement to ensure connectivity and drainage in an Urban Terrain. J. Hydrol. Eng 21, 06015017 10.1061/(ASCE)HE.1943-5584.0001306.

Barnes R, Callaghan KL, Wickert AD, 2019. Computing water flow through complex landscapes, part 2: finding hierarchies in depressions and morphological segmentations. Earth Surf. Dyn 1–19. 10.5194/esurf-2019-34.

Barnes R, Lehman C, Mulla D, 2014. Priority-flood: an optimal depression-filling and watershed-labeling algorithm for digital elevation models. Comput. Geosci 62, 117–127. 10.1016/J.CAGEO.2013.04.024.

Bertassello LE, Rao PSC, Jawitz JW, Aubeneau AF, Botter G, 2020. Wetlandscape hydrologic dynamics driven by shallow groundwater and landscape topography. Hydrol. Process 34, 1460–1474. 10.1002/hyp.13661.

Biggs J, von Fumetti S, Kelly-Quinn M, 2017. The importance of small waterbodies for biodiversity and ecosystem services: implications for policy makers. Hydrobiologia 793, 3–39. 10.1007/sl0750-016-3007-0.

Brooks JR, Mushet DM, Vanderhoof MK, Leibowitz SG, Christensen JR, Neff BP, Rosenberry DO, Rugh WD, Alexander LC, 2018. Estimating Wetland connectivity to streams in the prairie pothole region: an isotopic and remote sensing approach. Water Resour. Res 54, 955–977. 10.1002/2017WR021016.

Callow JN, Van Niel KP, Boggs GS, 2007. How does modifying a DEM to reflect known hydrology affect subsequent terrain analysis? J. Hydrol 332, 30–39. 10.1016/J.JHYDROL.2006.06.020.

Carlson R, Danner A, 2010. Bridge detection in grid terrains and improved drainage enforcement. In: Proceedings of the 18th SIGSPATIAL International Conference on Advances in Geographic Information Systems, pp. 250–259. 10.1145/1869790.1869827.

Cheng F, Basu NB, 2017. Biogeochemical hotspots: role of small water bodies in landscape nutrient processing. Water Resour. Res 53, 1–19. 10.1002/2016WR020102.

Chow V.Te, Ben-Zvi A, 1973. Hydrodynamic modeling of two-dimensional watershed flow. J. Hydraul. Div 99, 2023–2040. 10.1061/JYCEAJ.0003790.

Chu X, Yang J, Chi Y, Zhang J, 2013. Dynamic puddle delineation and modeling of puddle-to-puddle filling-spilling-merging-splitting overland flow processes. Water Resour. Res 49, 3825–3829. 10.1002/wrcr.20286.

Chu X, Zhang J, Chi Y, Yang J, 2010. An improved method for watershed delineation and computation of surface depression storage. Watershed Management 2010: Innovations in Watershed Management Under Land Use and Climate Change. American Society of Civil Engineer, pp. 1113–1122.

Cohen MJ, Creed IF, Alexander L, Basu NB, Calhoun AJK, Craft C, D'Amico E, DeKeyser E, Fowler L, Golden HE, Jawitz JW, Kalla P, Kirkman LK, Lane CR, Lang M, Leibowitz SG, Lewis DB, Marton J, McLaughlin DL, Mushet DM, Raanan-Kiperwas H, Rains MC, Smith L, Walls SC,

2016. Do geographically isolated wetlands influence landscape functions? Proc. Natl. Acad. Sci. U. S. A 113, 1978–1986. 10.1073/pnas.1512650113. [PubMed: 26858425]

Condon LE, Maxwell RM, 2019. Modified priority flood and global slope enforcement algorithm for topographic processing in physically based hydrologic modeling applications. Comput. Geosci 126, 73–83. 10.1016/J.CAGEO.2019.01.020.

Costabile P, Costanzo C, Gandolfi C, Gangi F, Masseroni D, 2022. Effects of DEM depression filling on river drainage patterns and surface runoff generated by 2D rain-on-grid scenarios. Water 14. 10.3390/wl4070997 (Switzerland).

Evenson GR, Golden HE, Lane CR, D'Amico E, 2016. An improved representation of geographically isolated wetlands in a watershed-scale hydrologic model. Hydrol. Process 30, 4168–4184. 10.1002/hyp.10930.

Gardner MA, Morton CG, Huntington JL, Niswonger RG, Henson WR, 2018. Input data processing tools for the integrated hydrologic model GSFLOW. Environ. Model. Softw 109, 41–53. 10.1016/j.envsoft.2018.07.020.

Golden HE, Creed IF, Ali G, Basu NB, Neff BP, Rains MC, McLaughlin DL, Alexander LC, Ameli AA, Christensen JR, Evenson GR, Jones CN, Lane CR, Lang M, 2017. Integrating geographically isolated wetlands into land management decisions. Front. Ecol. Environ 15, 319–327. 10.1002/fee.1504. [PubMed: 30505246]

Golden HE, Lane CR, Amatya DM, Bandilla KW, Raanan Kiperwas H, Knightes CD, Ssegane H, 2014. Hydrologic connectivity between geographically isolated wetlands and surface water systems: a review of select modeling methods. Environ. Model. Softw 53, 190–206. 10.1016/J.ENVSOFT.2013.12.004.

GRASS Development Team, 2020. Geographic Resources Analysis Support System (GRASS) software.

Hart PE, Nilsson NJ, Raphael B, 1968. A formal basis for the heuristic determination of minimum cost paths. IEEE Trans. Syst. Sci. Cybern 4, 100–107. 10.1109/TSSC.1968.300136.

Hay L, Norton P, Viger R, Markstrom S, Steven Regan R, Vanderhoof M, 2018. Modelling surface-water depression storage in a Prairie Pothole Region. Hydrol. Process 32, 462–479. 10.1002/hyp.11416.

Hengl T, 2006. Finding the right pixel size. Comput. Geosci 32, 1283–1298. 10.1016/J.CAGEO.2005.11.008.

Hodges BR, 2015. Representing hydrodynamically important blocking features in coastal or riverine lidar topography. Nat. Hazards Earth Syst. Sci 15, 1011–1023. 10.5194/nhess-15-1011-2015.

Iserles A, 2009. A First Course in the Numerical Analysis of Differential Equations, 2nd ed. Cambridge University Press, New York.

Jan A, Coon ET, Graham JD, Painter SL, 2018. A subgrid approach for modeling microtopography effects on overland flow. Water Resour. Res 54, 6153–6167. 10.1029/2017WR021898.

Jones CN, Ameli A, Neff BP, Evenson GR, McLaughlin DL, Golden HE, Lane CR, 2019. Modeling connectivity of non-floodplain Wetlands: insights, approaches, and recommendations. J. Am. Water Resour. Assoc 55, 559–577. 10.1111/1752-1688.12735. [PubMed: 34316250]

Jones CN, Evenson GR, McLaughlin DL, Vanderhoof MK, Lang MW, McCarty GW, Golden HE, Lane CR, Alexander LC, 2018. Estimating restorable wetland water storage at landscape scales. Hydrol. Process 32, 305–313. 10.1002/hyp.11405. [PubMed: 29681686]

Jones JE, Woodward CS, 2001. Newton-Krylov-multigrid solvers for large-scale, highly heterogeneous, variably saturated flow problems. Adv. Water Resour 24, 763–774. 10.1016/S0309-l708(00)00075-0.

Kollet SJ, Maxwell RM, 2006. Integrated surface–groundwater flow modeling: a free-surface overland flow boundary condition in a parallel groundwater flow model. Adv. Water Resour 29, 945–958. 10.1016/J.ADVWATRES.2005.08.006.

Leibowitz PJW Jr, S.G., Schofield KA, Alexander LC, Vanderhoof K, Golden HE, 2019. Connectivity of streams and wetlands to downstream waters: an integrated systems framework J. Am. Water Resour. Assoc 54, 1–42. 10.1111/1752-1688.12631.

Li S, MacMillan RA, Lobb DA, McConkey BG, Moulin A, Fraser WR, 2011. Lidar DEM error analyses and topographic depression identification in a hummocky landscape in the prairie region of Canada. Geomorphology 129, 263–275. 10.1016/j.geomorph.2011.02.020.

Lidberg W, Nilsson M, Lundmark T, Ågren AM, 2017. Evaluating preprocessing methods of digital elevation models for hydrological modelling. Hydrol. Process 31, 4660–4668. 10.1002/hyp.11385.

Lindsay JB, 2016a. The practice of DEM stream burning revisited. Earth Surf. Process. Landforms 41, 658–668. 10.1002/esp.3888.

Lindsay JB, 2016b. Efficient hybrid breaching-filling sink removal methods for flow path enforcement in digital elevation models. Hydrol. Process 30, 846–857. 10.1002/hyp.10648.

Lindsay JB, Creed IF, 2005. Removal of artifact depressions from digital elevation models: towards a minimum impact approach. Hydrol. Process 19, 3113–3126. 10.1002/hyp.5835.

Liu G, Schwartz FW, 2011. An integrated observational and model-based analysis of the hydrologic response of prairie pothole systems to variability in climate. Water Resour. Res 47 10.1029/2010WR009084.

Liu G, Schwartz FW, Wright CK, McIntyre NE, 2016. Characterizing the climate-driven collapses and expansions of wetland habitats with a fully integrated surface-subsurface hydrologic model. Wetlands 36, 287–297. 10.1007/S13157-016-0817-9.

Maxwell RM, 2013. A terrain-following grid transform and preconditioner for parallel, large-scale, integrated hydrologic modeling. Adv. Water Resour 53, 109–117. 10.1016/J.ADVWATRES.2Oi2.lO.OOl.

Metz M, Mitasova H, Harmon RS, 2011. Efficient extraction of drainage networks from massive, radar-based elevation models with least cost path search. Hydrol. Earth Syst. Sci 15, 667–678. 10.5194/hess-15-667-2011.

Minakawa N, Mutero CM, Githure JI, Beier JC, Yan G, 1999. Spatial distribution and habitat characterization of anopheline mosquito larvae in western Kenya. Am. J. Trop. Med. Hyg 61, 1010–1016. 10.4269/ajtmh.1999.61.1010. [PubMed: 10674687]

Moreno-Gómez M, Liedl R, Stefan C, 2019. A new GIS-based model for karst dolines mapping using LiDAR; application of a multidepth threshold approach in the Yucatan Karst, Mexico. Remote Sens. 11, 1147. 10.3390/rslll01147.

Nasab MT, Chu X, 2020. Macro-HyProS: a new macro-scale hydrologic processes simulator for depression-dominated cold climate regions. J. Hydrol 580, 124366 10.1016/j.jhydrol.2019.124366.

Nasab MT, Zhang J, Chu X, 2017. A new depression-dominated delineation (D-cubed) method for improved watershed modelling. Hydrol. Process 31, 3364–3378. 10.1002/hyp.11261.

Planchon O, Darboux F, 2001. A fast , simple and versatile algorithm to fill the depressions of digital elevation models. Catena 46, 159–176.

Rajib A, Golden HE, Lane CR, Wu Q, 2020. Surface depression and wetland water storage improves major river basin hydrologic predictions. Water Resour. Res 56, e2019WR026561 10.1029/2019wr026561.

Rieger W, 1998. A phenomenon-based approach to upslope contributing area and depressions in DEMs. Hydrol. Process 12, 857–872. 10.1002/(SICI)1099-1085(199805)12:6.

Sanders BF, 2007. Evaluation of on-line DEMs for flood inundation modeling. Adv. Water Resour 30, 1831–1843. 10.1016/j.advwatres.2007.02.005.

Sanders BF, Schubert JE, 2019. PRIMo: parallel raster inundation model. Adv. Water Resour 126, 79–95. 10.1016/j.advwatres.2019.02.007.

Schwanghart W, Scherler D, 2017. Bumps in river profiles: uncertainty assessment and smoothing using quantile regression techniques. Earth Surf. Dyn 5, 821–839. 10.5194/esurf-5-821-2017.

Tavares da Costa R, Mazzoli P, Bagli S, 2019. Limitations posed by free DEMs in watershed studies: the case of river Tanaro in Italy. Front. Earth Sci 7, 141. 10.3389/feart.2019.00141.

Wang N, Chu X, 2020. A new algorithm for delineation of surface depressions and channels. Water 12, 7. 10.3390/wl2010007 (Basel).

Wang N, Chu X, Zhang X, 2021. Functionalities of surface depressions in runoff routing and hydrologic connectivity modeling. J. Hydrol 593, 125870 10.1016/j.jhydrol.2020.125870.

Wang L, Liu H, 2006. An efficient method for identifying and filling surface depressions in digital elevation models for hydrologic analysis and modelling. Int. J. Geogr. Inf. Sci 20, 193–213. 10.1080/13658810500433453.

Woodrow K, Lindsay JB, Berg AA, 2016. Evaluating DEM conditioning techniques, elevation source data, and grid resolution for field-scale hydrological parameter extraction. J. Hydrol 540, 1022–1029. 10.1016/J.JHYDROL.2016.07.018.

Wu Q, Deng C, Chen Z, 2016. Automated delineation of karst sinkholes from LiDAR-derived digital elevation models. Geomorphology 266, 1–10. 10.1016/J.GEOMORPH.2016.05.006.

Wu Q, Lane CR, Wang L, Vanderhoof MK, Christensen JR, Liu H, 2019. Efficient delineation of nested depression hierarchy in digital elevation models for hydrological analysis using level-set method. J. Am. Water Resour. Assoc 55, 354–368. 10.1111/1752-1688.12689. [PubMed: 33776405]

Yang J, Chu X, 2015. A new modeling approach for simulating microtopography-dominated, discontinuous overland flow on infiltrating surfaces. Adv. Water Resour 78, 80–93. 10.1016/j.advwatres.2015.02.004.

Yasarer LMW, Bingner RL, Momm HG, 2018. Characterizing ponds in a watershed simulation and evaluating their influence on streamflow in a Mississippi watershed. Hydrol. Sci. J 63, 302–311. 10.1080/02626667.2018.1425954.

Yu CW, Hodges BR, Liu F, 2020. A new form of the Saint-Venant equations for variable topography. Hydrol. Earth Syst. Sci 24, 4001–4024. 10.5194/hess-24-4001-2020.

Zeng L, Shao J, Chu X, 2020. Improved hydrologic modeling for depression-dominated areas. J. Hydrol 590, 125269 10.1016/j.jhydrol.2020.125269.

Zhang W, Cundy TW, 1989. Modeling of two-dimensional overland flow. Water Resour. Res 25, 2019–2035. 10.1029/WR025I009P02019.

Zhu D, Ren Q, Xuan Y, Chen Y, Cluckie ID, 2013. An effective depression filling algorithm for DEM-based 2-D surface flow modelling. Hydrol. Earth Syst. Sci 17, 495–505. 10.5194/hess-17-495-2013.

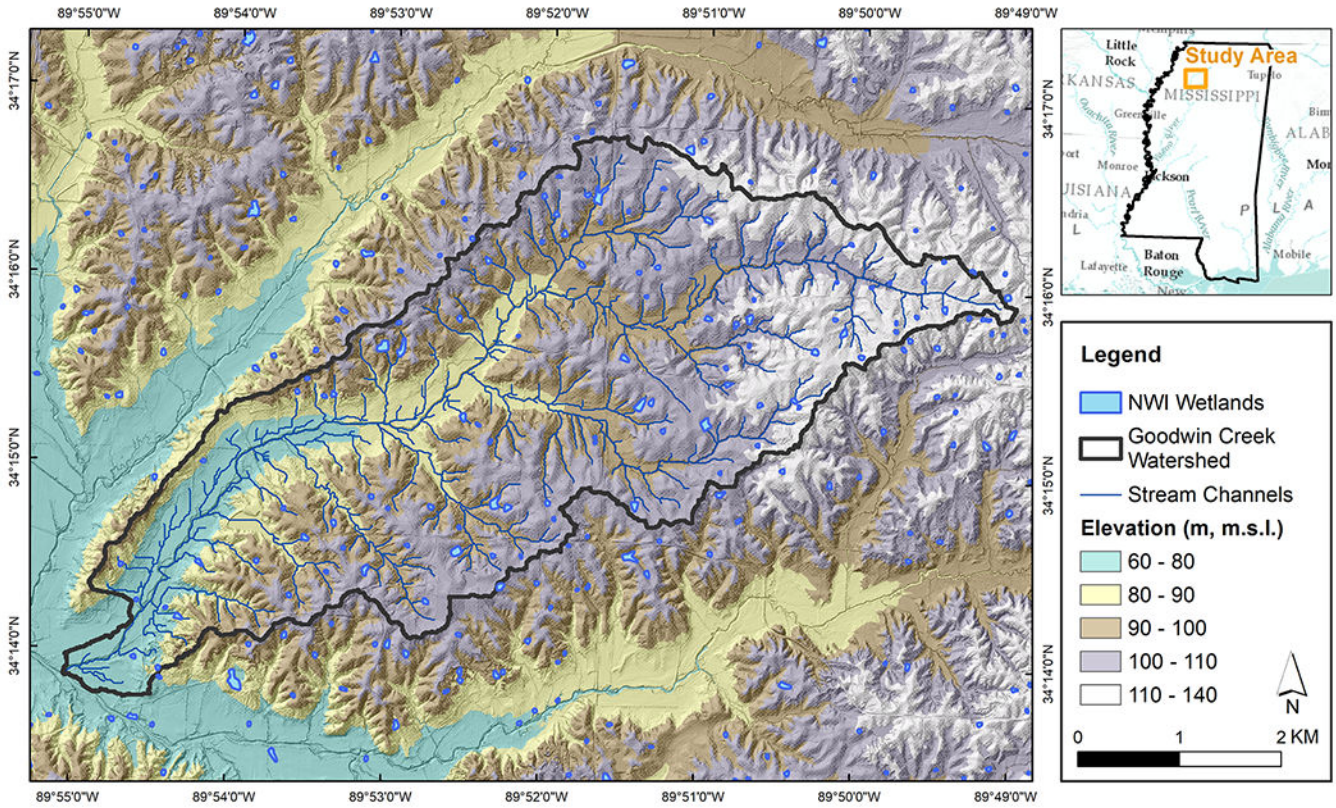

Fig. 1.
Goodwin Creek Experimental Watershed (GCEW) study area.

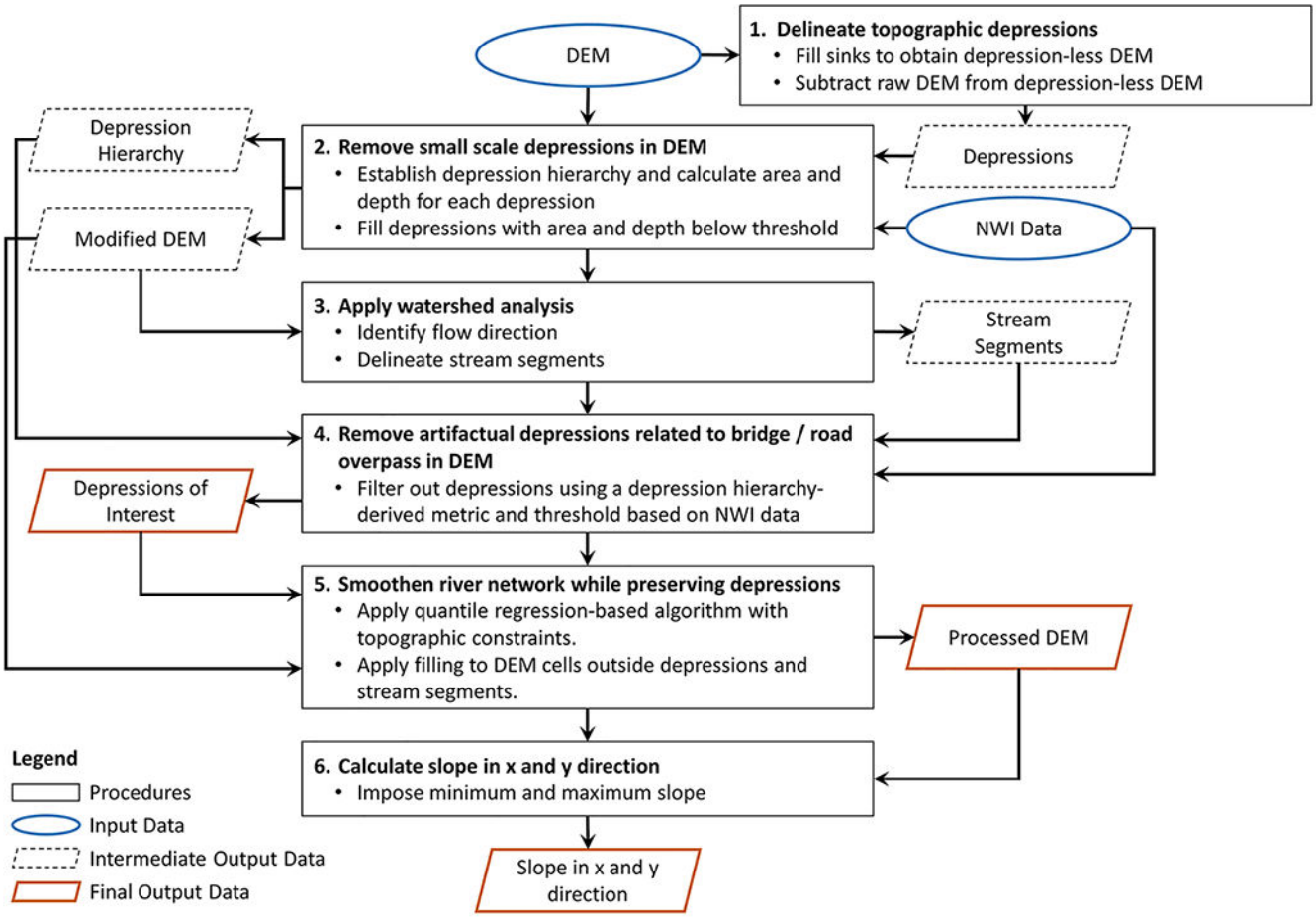

Fig. 2.

Schematic flowchart for the proposed Depression-preserved DEM Processing (D2P) algorithm.

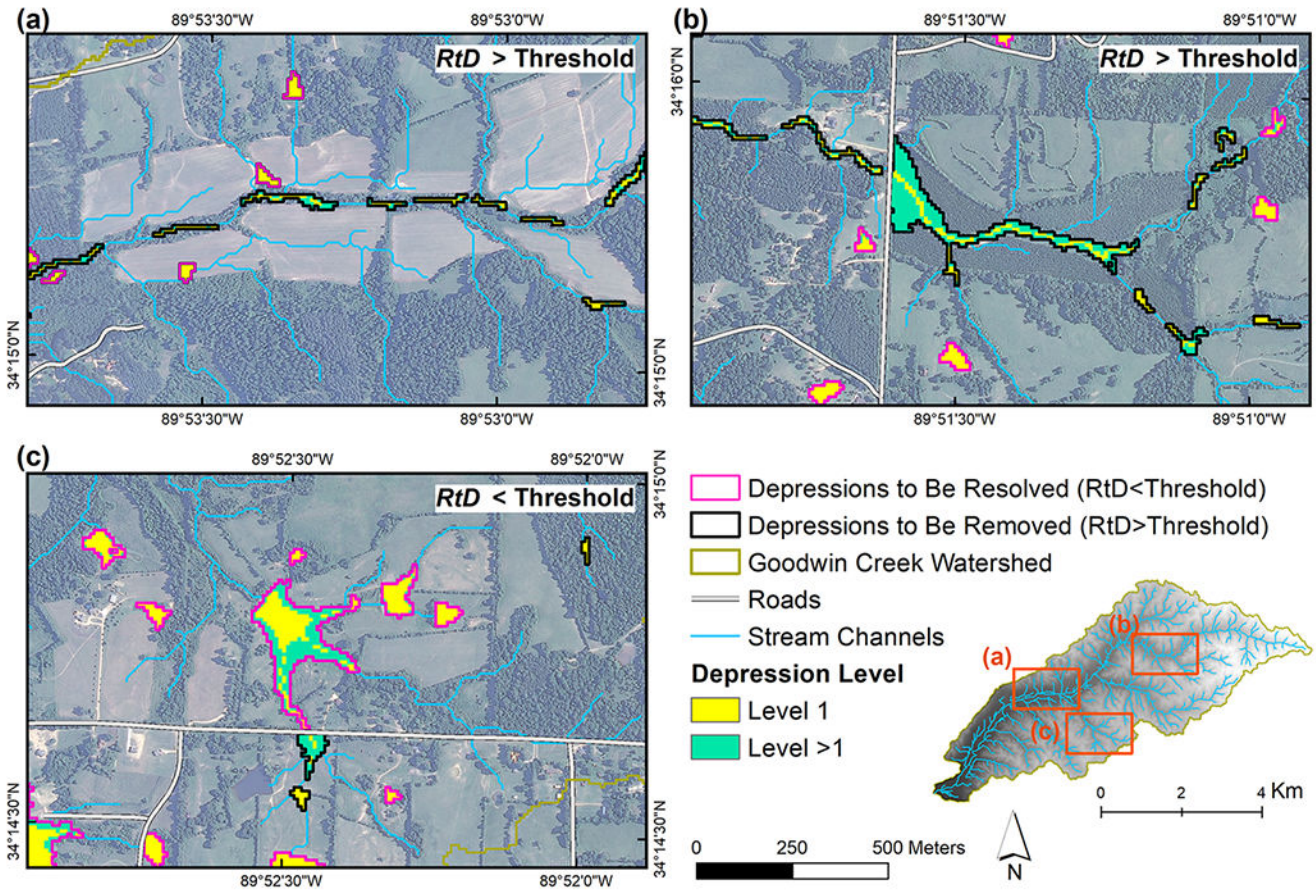

Fig. 3.

Examples of (a) depression within channel width, (b) false depression at road/bridge overpass (c) water bodies partially coinciding with river within GCEW.

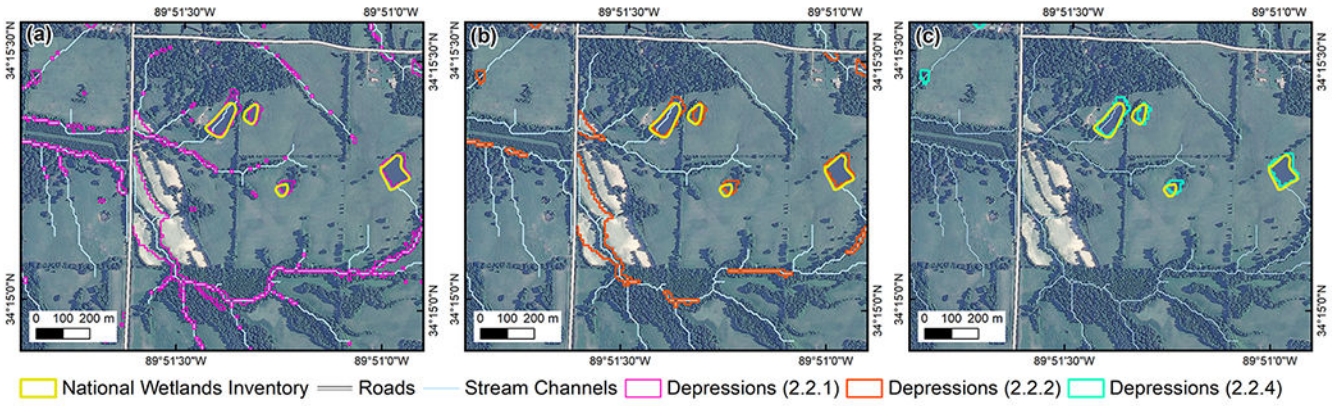

Fig. 4.

Illustration of gradual exclusion of select depressions in GCEW study area. (a) Delineated sinks from Section 2.2.1. (b) Post-removal of small-scale depressions from Section 2.2.2. (c) Remaining depressions after the removal of depressions within the channel width and depressions associated with false hydrologic barriers from Section 2.2.4.

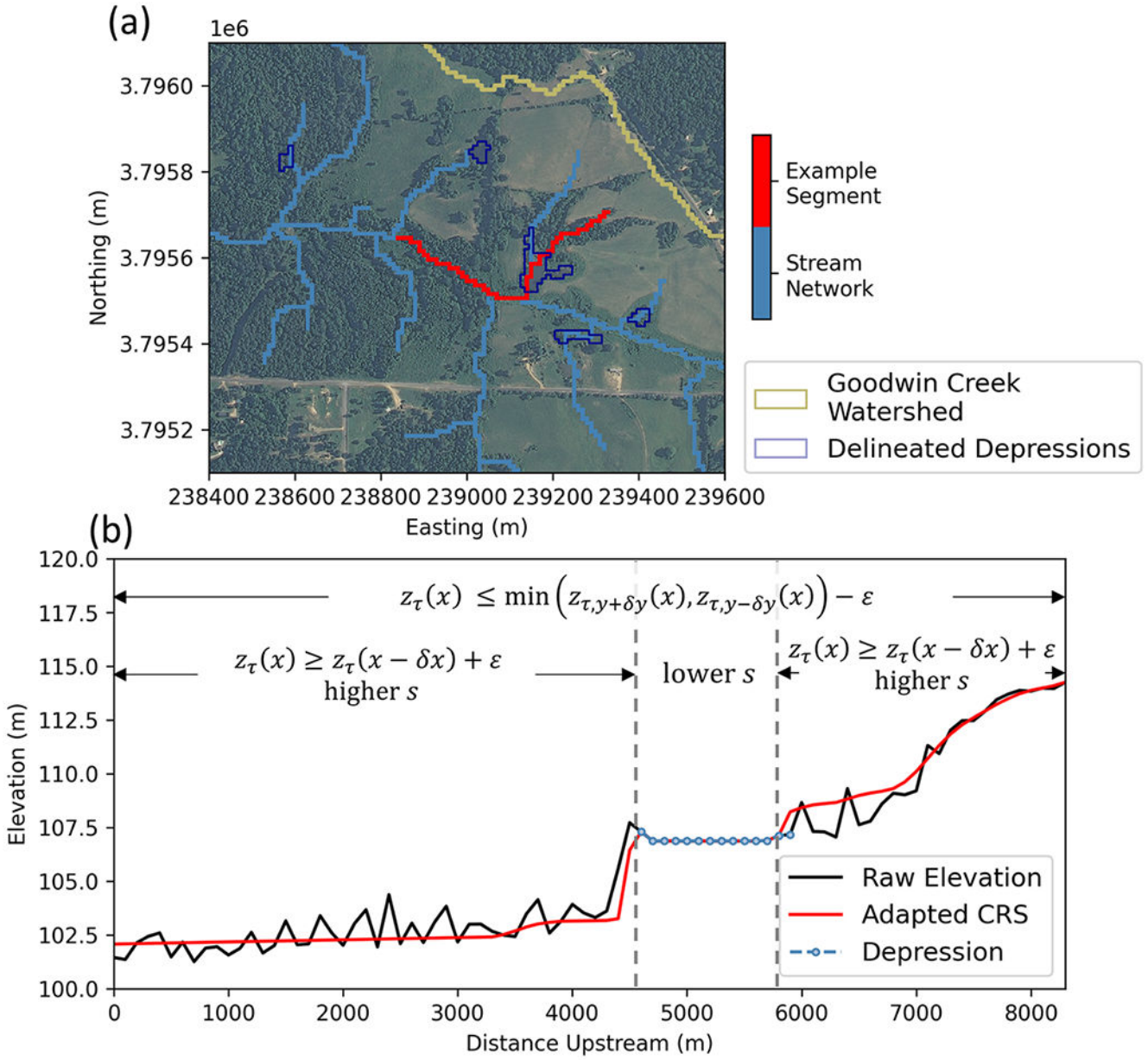

Fig. 5.

Illustration of adapted CRS for smoothening of an example river segment in GCEW study area. (a) Plan view of river segment in red coinciding with a depression delineated in dark blue. (b) Corresponding elevation profile of river segment from (a) before and after the implementation of the adapted CRS for river smoothening. A downstream slope was enforced on the river except the segment within the depression. The elevation of the rivers segment was globally set not to exceed that of the riverbanks and a lower degree of smoothening was applied on the river segment within the depression.

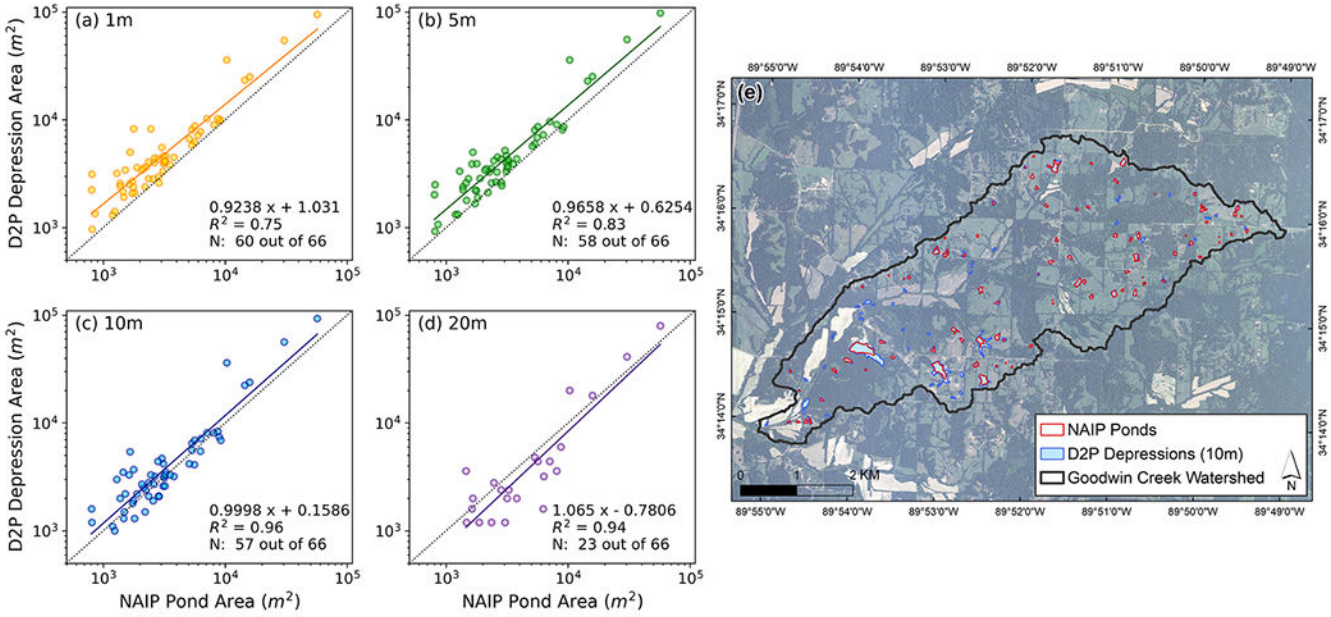

Fig. 6.

Scatter plot of area of depressions identified by D2P against that of the manually delineated ponds from NAIP imagery at DEM resolutions of (a) 1 m, (b) 5 m, (c) 10 m and (d) 20 m. (e) Comparison of spatial distribution of NAIP ponds and D2P depressions using DEM resolution of 10 m. N is the number of D2P depressions coinciding with NAIP ponds (out of a total of 66 ponds).

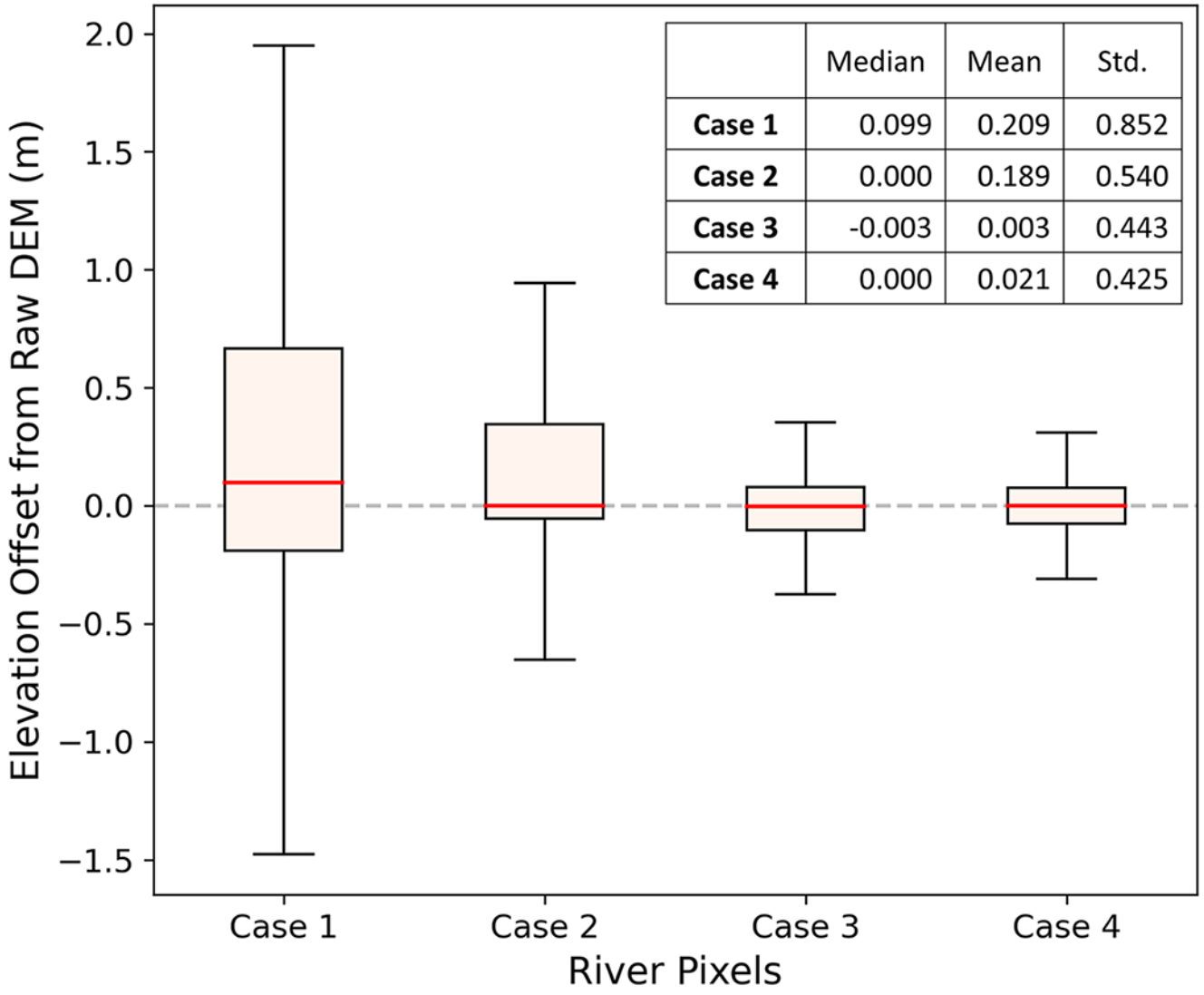

Fig. 7.

Boxplot of elevation offset from raw DEM of the grid cells in the river network for the four cases. The median is represented by the red line in the box. Outliers have been removed.

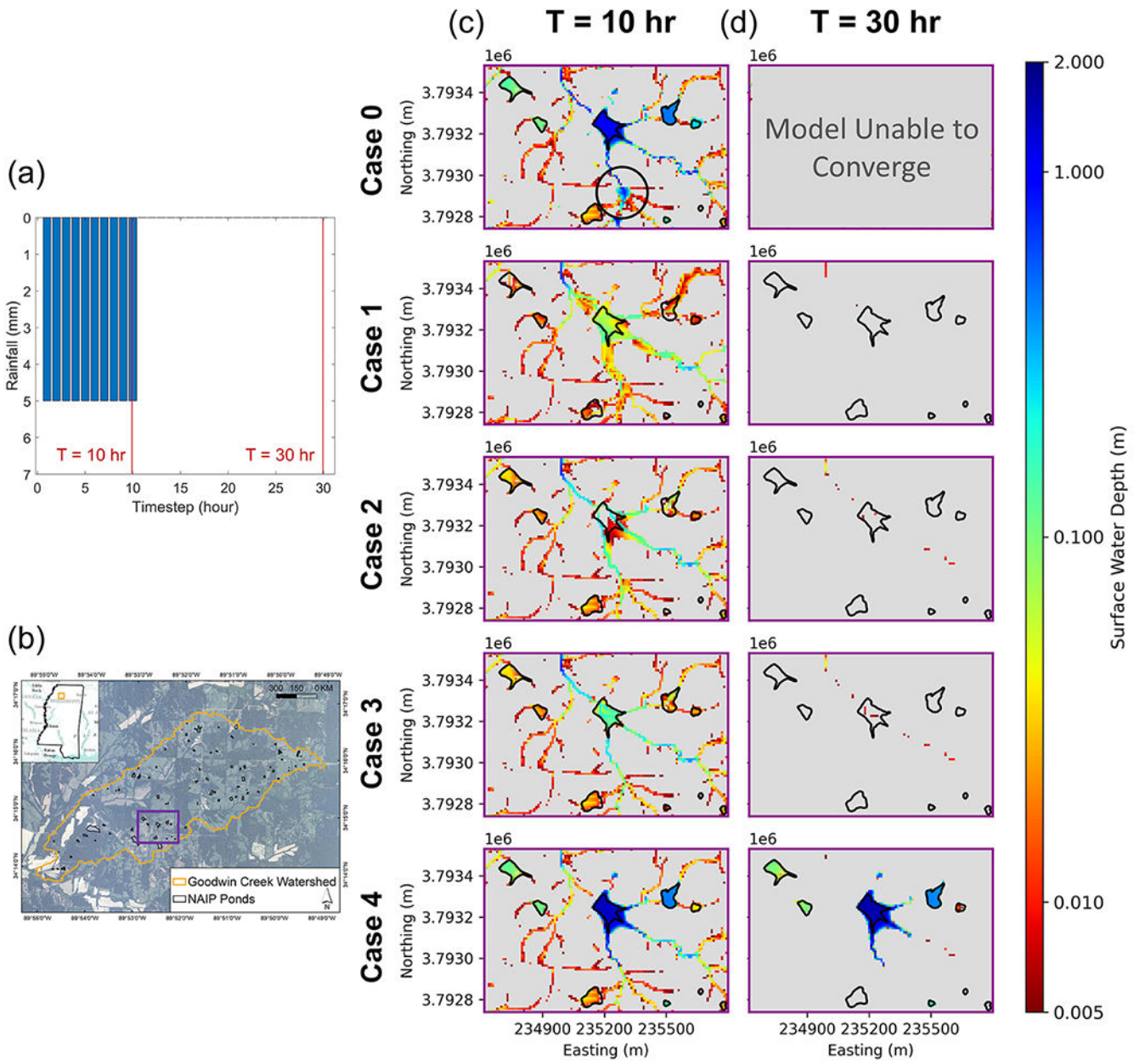

Fig. 8.

Example surface water depth map from two-time instants at a selected location for the simulations using the raw DEM (Case 0) and four DEM processing approaches (Case 1–4). (a) Rainfall hyetograph in ParFlow simulation (b) Watershed map showing selected location in purple box and distribution of benchmark depressions extracted from NAIP (c) Surface water depth map 10 hrs into the simulation (d) Surface water depth map 30 hrs into the simulation.

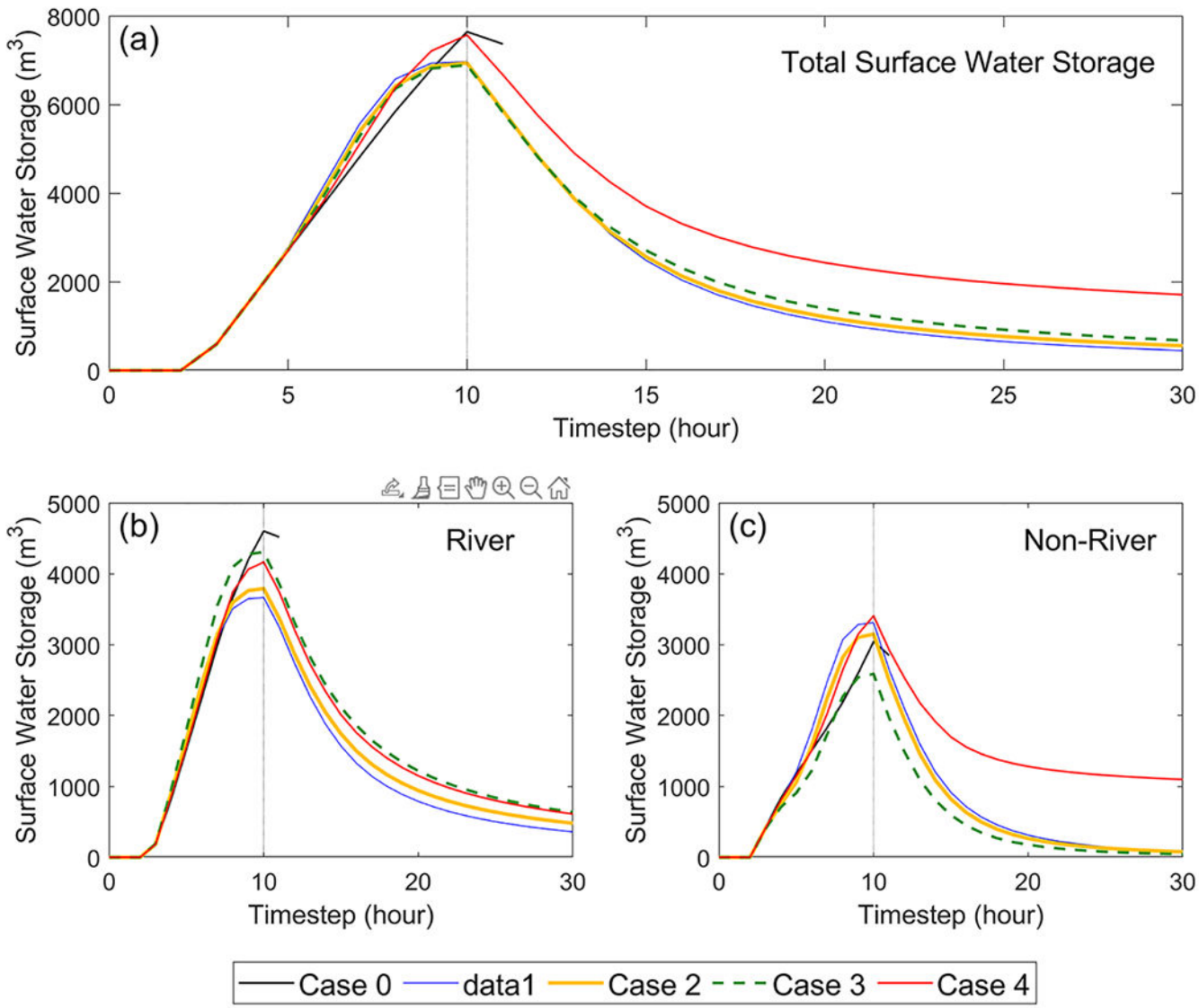

Fig. 9.

Time series of the surface water storage for the simulations using raw DEM (Case 0) and four DEM processing approaches (Case 1–4). (a) Total surface water storage (b) Surface water storage in river cells (c) Surface water storage in non-river cells.

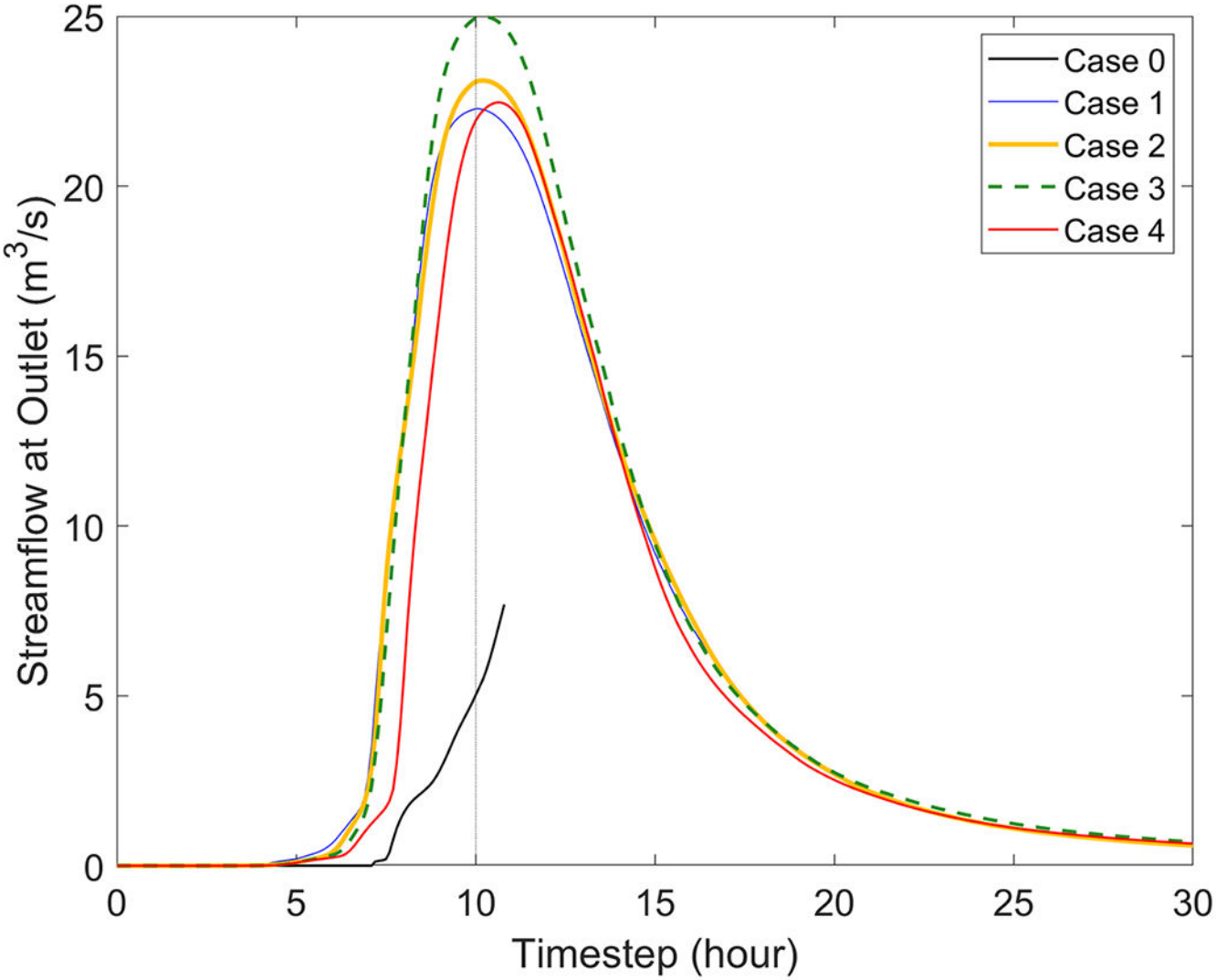

Fig. 10.
Hydrograph at the outlet of GCEW for the simulations using the raw DEM (Case 0) and four DEM processing approaches (Case 1–4).

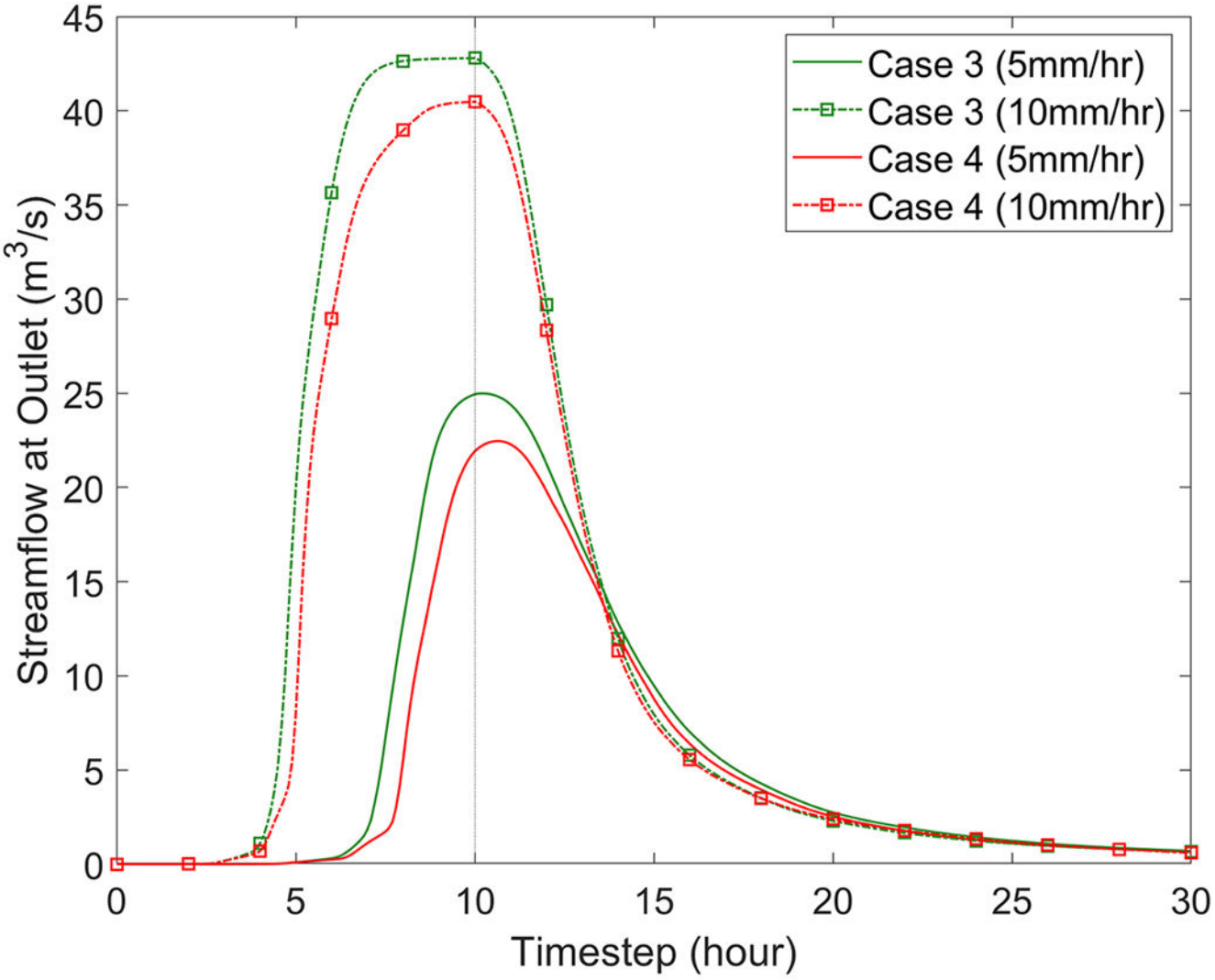

Fig. 11.
Comparison of hydrograph between Case 3 (depression-less) and Case 4 (depression integrated) at different rainfall rates.

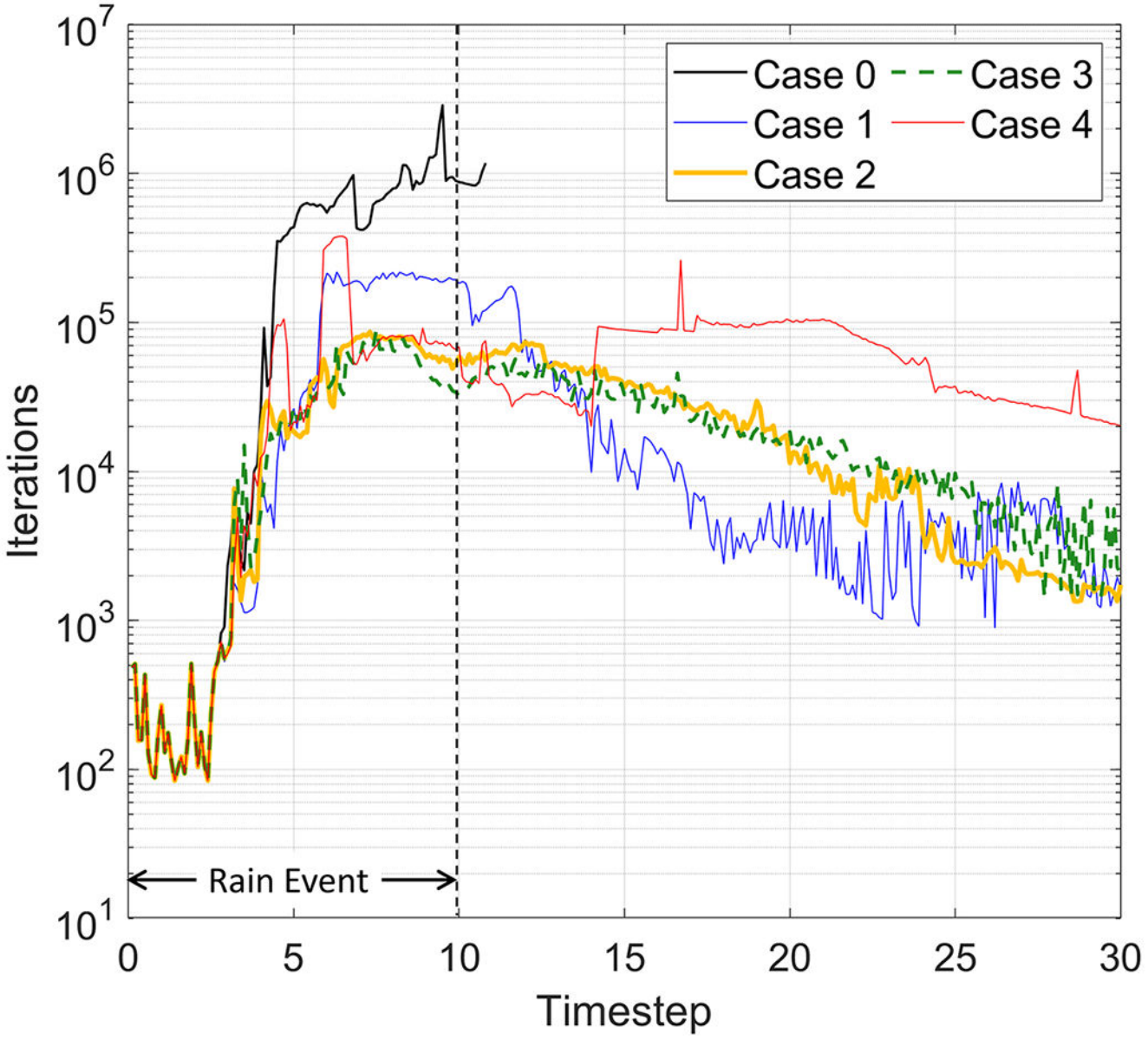

Fig. 12.
Comparison of number of solver iterations in ParFlow for each time step across the cases.

Table 1

Summary of DEM processing methods used for the comparison.

	Description	Depression Treatment	River Smoothening	Depression Preserved
Case 0	Raw DEM	None	No	Yes
Casel	Conventional algorithm (Condon et al., 2019)	Filling	Yes (Constant Slope)	No
Case 2	Case 1 + improved stream smoothing	Filling	Yes (Adapted CRS – uniform decreasing elevation downstream)	No
Case 3	Case 2 + reduced modification to DEM	Breaching/filling during river smoothening + Post-filling	Yes (Adapted CRS – uniform decreasing elevation downstream)	No
Case 4	Proposed algorithm (D2P)	Selective filling of small-scale depressions + Breaching/filling of depressions within channel width and false depressions during river smoothening	Yes (Adapted CRS – uniform decreasing elevation downstream except at preserved depressions)	Yes (Select Depressions)

Table 2

Statistical binary comparison of D2P depressions against rasterized NAIP ponds across the different DEM resolutions. The definition of probability of detection (POD), false alarm rate (FAR) and critical success index (CSI) can be found in Supporting Information Text S5.

Resolution	POD	FAR	CSI
1 m	0.92	0.47	0.50
5 m	0.89	0.46	0.50
10 m	0.86	0.44	0.52
20 m	0.49	0.53	0.32

Table 3

Statistics of modified cells and absolute elevation offset compared to the raw DEM based on all grid cells in the watershed for the four cases. The values in the bracket are the statistics for only the grid cells in the river network.

DEM Conditioning Method	Elevation	
	% Of Modified Cells	Mean Absolute Elevation Offset (m)
Case 1	11.3 (97.1)	0.0745 (0.648)
Case 2	8.40 (34.0)	0.0394 (0.328)
Case 3	6.35 (33.3)	0.0160 (0.240)
Case 4	5.58 (30.6)	0.0145 (0.223)

Table 4

Statistics of channel slope and channel depth of GCEW calculated from the raw DEM (Case 0) and conditioned DEMs (Case 1 to 4).

DEM Conditioning Method	Channel Slope (−)		Channel Depth (m)	
	Mean	Std.	Mean	Std.
Case 0	−0.016	0.051	0.50	0.72
Case 1	−0.014	0.010	0.39	0.71
Case 2	−0.014	0.015	0.38	0.49
Case 3	−0.015	0.016	0.50	0.63
Case 4	−0.015	0.019	0.49	0.63